Fast Frequency Response From Offshore Multiterminal VSC–HVDC Schemes

Oluwole Daniel Adeuyi, *Member, IEEE*, Marc Cheah-Mane, *Student Member, IEEE*, Jun Liang, *Senior Member, IEEE*, and Nick Jenkins, *Fellow, IEEE*

***Abstract*—This paper analyzes the frequency support characteristics of multiterminal voltage source converter HVdc (VSC–HVdc) (MTDC) schemes using the energy transferred from wind turbine rotating mass and other ac systems. An alternative coordinated control (ACC) scheme that gives priority to a frequency versus active power droop fitted to onshore VSCs is proposed to: transfer wind turbine recovery power to undisturbed ac grids, and allow correct control operation of MTDC systems during multiple power imbalances on different ac grids. The fast frequency response capability of MTDC systems equipped with the proposed ACC scheme is compared against a coordinated control scheme, which uses a frequency versus dc voltage droop. The frequency control schemes are demonstrated on an experimental test rig, which represents a three-terminal HVdc system. Also, the MTDC frequency support capability when wind farms do not provide extra power is tested using a four-terminal HVdc system.**

***Index Terms*—Frequency control, hardware-in-the-loop simulation, inertial response, multi-terminal VSC-HVDC (MTDC) transmission, offshore wind farm.**

I. Introduction

VARIABLE speed wind turbines and other low carbon generators and loads, that are connected through power converters, do not inherently contribute to the inertia of power systems, unless they are fitted with supplementary controls [1], [2], [3]. Multi-terminal high voltage direct current (MTDC) systems, based on voltage source converter (VSC) technology, are intended to transfer the power generated from offshore wind farms to onshore grids and interconnect the grids of different countries for electricity trading. The active power transferred from MTDC systems will replace conventional synchronous generation capacity on onshore AC grids, reduce system inertia and increase the risk of operation and frequency control on the AC grids [1].

During a frequency disturbance, a power system with low inertia will have a higher Rate of Change of Frequency (RoCoF) and require additional energy to contain the frequency within operational limits, than a power system with high inertia [1]. This increase in the rate of change of frequency may result in unintended tripping of distributed generators with loss of mains relays. Also, the actions required to contain the frequency would need to take place more rapidly to avoid loss of synchronism [4]. Variable speed wind turbines and HVDC links fitted with auxiliary controls are capable of providing fast frequency response to AC grids with low inertia [1].

The authors in [5]–[7] reported two methods for provision of fast frequency response from wind turbines. These are: (i) kinetic energy from wind turbine rotating mass; and (ii) additional active power from wind turbines operating in de-loaded condition. The kinetic energy is delivered to AC grids more rapidly than the de-loading operation. For the case of kinetic energy extraction, the generator rotor speed decreases and the kinetic energy stored in the wind turbine rotating mass is used to provide additional power to the AC grids. Once the wind turbine inertia support has ended, the generator rotor speed will have to recover back to its original value within a period of time, known as the recovery period [8], [9]. Wind turbines operating at below rated wind speed will experience a temporary under-production of power during their recovery period. The recovery power will result in a further loss of power and produce a further frequency drop on disturbed AC grids, after an initial power imbalance [10], [5].

Two methods for provision of fast frequency response from point-to-point (P2P) HVDC links were proposed in [1], [6], [11], [12]: (i) additional active power from other AC systems and (ii) electrostatic energy from DC link capacitors. The authors in [13] proposed a communication-free coordinated control (CC) scheme that allows frequency response from P2P HVDC-connected offshore wind farms. The CC scheme uses a supplementary frequency versus DC voltage droop at the onshore VSCs and a DC voltage versus offshore frequency droop at the offshore converters for fast frequency response from the offshore wind farms. An inertia emulation control scheme was presented in [14], to utilize the electrostatic energy stored in the HVDC links, but this required large DC link capacitors [6]. A frequency control strategy, which utilizes the energy from wind turbines and DC capacitors of the P2P HVDC links for frequency support was developed in [15] and analysed in [6].

The CC scheme was applied to MTDC-connected offshore wind farms in [16], but the DC voltage versus frequency droop

Manuscript received July 5, 2016; revised September 29, 2016; accepted November 17, 2016. Date of publication December 5, 2016; date of current version October 16, 2017. This work was supported in part by the RCUK HubNet under Grant EP/I013636/1, in part by the Top and Tail Programme (EP/I031707/1), in part by the EU FP7 Programme, in part by the MEDOW Project (317221), and in part by the EPSRC under Grant EP/L024155/1. Paper no. TPWRD-00849-2016.

The authors are with the School of Engineering, Cardiff University, Cardiff CF24 3AA, U.K. (e-mail: AdeuyiOD@cardiff.ac.uk; CheahM@cardiff.ac.uk; LiangJ1@cardiff.ac.uk; JenkinsN6@cardiff.ac.uk).

Color versions of one or more of the figures in this paper are available online at http://ieeexplore.ieee.org.

Digital Object Identifier 10.1109/TPWRD.2016.2632860

on offshore VSCs resulted in maloperation of wind farm frequency response during multiple power imbalances on different AC grids [5]. A weighted frequency scheme was proposed to restore correct operation of wind turbine frequency response during multiple power imbalances on different AC grids, but this required fast telecommunications between VSCs [5]. The authors in [17], [18] proposed a communication-free dual controller, which combines a frequency versus power droop with the DC voltage droop fitted on onshore VSCs of MTDC systems. Interactions between the direct voltage droop and frequency droop of the dual controller was investigated in [19]. A droop correction factor was proposed in [20] to avoid the droop interactions, by manipulating the frequency droop gain of the dual controller. However, the droop correction factor depends on the DC voltage droop information of all the onshore converters [20], which requires fast telecommunications between VSCs. Also, the temporary under-production of power due to the wind turbine recovery period resulted in a further frequency drop on the disturbed AC grid connected to VSCs equipped with the dual frequency controller [21].

In this paper, a communication-free alternative coordinated control (ACC) scheme is developed to: (i) prevent further frequency drop on disturbed AC grids during wind turbine recovery period and (ii) allow correct operation of wind turbine frequency response during multiple power imbalances. The proposed ACC scheme gives priority to the frequency versus power droop of dual controllers and deactivates the direct voltage droop during fast frequency response from MTDC systems, in order to eliminate interactions between the two droops. A 3-terminal HVDC system modelled using PSCAD and implemented on a hardware-in-the-loop experimental test rig is used to demonstrate the effectiveness of the proposed ACC scheme and the results are compared with the CC scheme. The MTDC frequency support capability when wind farms do not provide extra power is demonstrated using a 4-terminal system modelled using MATLAB Simulink.

II. Frequency Support Control For MTDC Systems

During normal operation, onshore grid-side converters (GSCs) of MTDC systems typically use a vector control strategy, in which the d-axis regulates the direct voltage (P vs. $V_{\rm dc}$ droop) or the active power ($V_{\rm dc}$ vs. P droop) and the q-axis controls reactive power, Q. Fig. 1 shows the structure of the outer loop and inner loop controllers of the GSCs in normal operation. The outer loops use PI controllers to compute the reference values of current, i_d^* and i_q^*, which are fed to the inner loop as illustrated in Fig. 1.

In an MTDC scheme with multiple onshore AC systems and offshore wind farms, a power imbalance on the onshore AC system will cause a frequency variation. Local measurements at each terminal [16] or telecommunication schemes [5] are used to transmit the information of the frequency variation to the VSCs of the MTDC scheme. These converters are controlled to provide frequency response from the energy sources of the MTDC scheme.

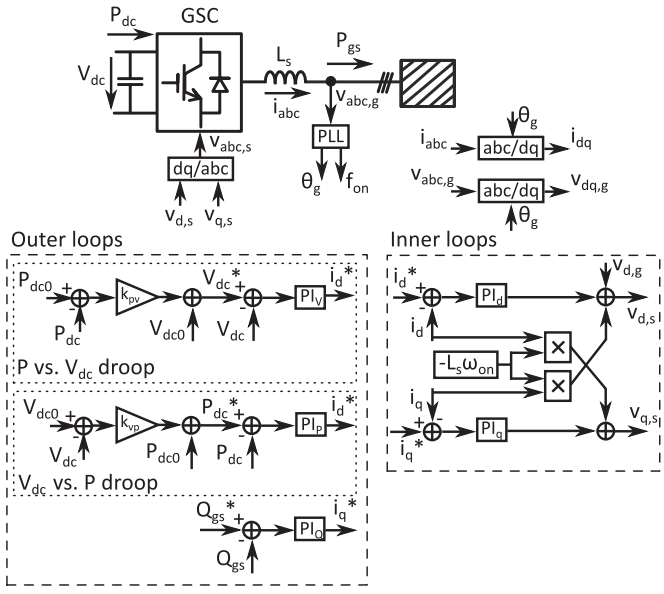

Fig. 1. Control diagram for grid-side converters in normal operation.

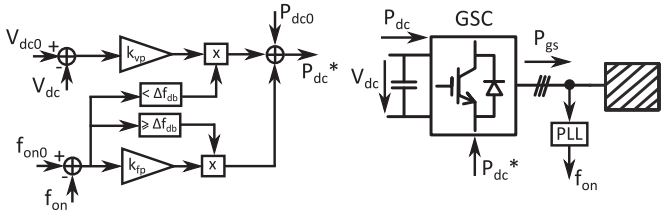

Fig. 2. Control diagram for grid-side converters with the CC scheme.

A. Coordinated Control Scheme

The CC scheme is designed by fitting a supplementary frequency versus DC voltage (f vs. $V_{\rm dc}$) droop to onshore grid-side converter (GSC) controllers and a DC voltage versus frequency ($V_{\rm dc}$ vs. f) droop to offshore wind farm converter (WFC) controllers [16].

1) GSCs with CC Scheme: the control operation of the onshore converters is:

$$V_{\rm dc}^* = V_{\rm dc0} - k_{\rm pv}(P_{\rm dc0} - P_{\rm dc}) + k_f \overbrace{(f_{\rm on0} - f_{\rm on})}^{\Delta f_{\rm on}} \quad (1)$$

where $k_{\rm pv}$ is the gain of an active power versus DC voltage (P vs. $V_{\rm dc}$) droop and k_f is the gain of the f vs. $V_{\rm dc}$ droop control system. Fig. 2 shows the control system fitted to the GSCs of the CC scheme.

During normal operation, the frequency deviation, $\Delta f_{\rm on}$ in (1) is 0 and the P vs. $V_{\rm dc}$ droop regulates DC voltage and transfers active power variations to onshore converters of the MTDC system. During a power imbalance on the AC grids, the system frequency, $f_{\rm on}$, starts to deviate from its nominal value, $f_{\rm on0}$, and the frequency deviation, $|\Delta f_{\rm on}|$, starts to increase. The disturbed AC grid model includes an aggregated inertia, $H_{\rm sys}$, self-load regulation effect, D, and primary frequency response of synchronous generators [22].

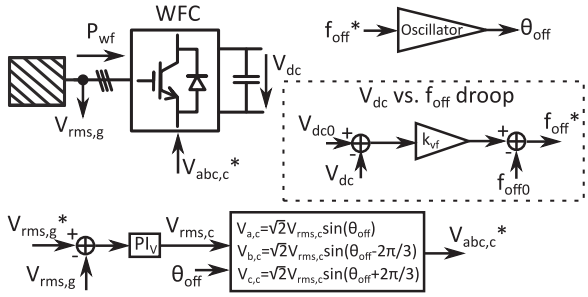

Fig. 3. Control diagram for WFC with frequency support schemes.

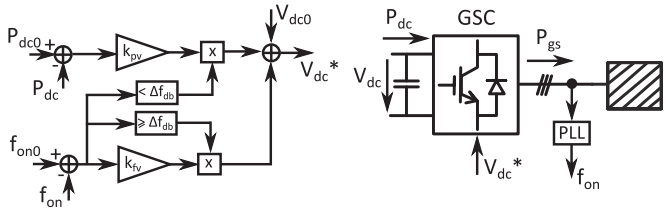

Fig. 4. Control diagram for grid-side converters with the ACC scheme.

When $|\Delta f_{\rm on}|$ is above a specific margin, $|\Delta f_{\rm db}|$, onshore converters connected to the disturbed AC grid will detect the frequency variations and switch from the original P vs. $V_{\rm dc}$ droop to the f vs. $V_{\rm dc}$. The f vs. $V_{\rm dc}$ controller uses the frequency variations on disturbed AC grids to regulate the reference value of the DC voltage, $V_{\rm dc}$, on the MTDC grid (where $k_{\rm pv}=0$ in (1)). The new control operation in the onshore converters of MTDC systems with the CC scheme is:

$$\begin{cases} V^*_{{\rm dc},i} = V_{{\rm dc0},i} - k_{{\rm pv},i}(P_{{\rm dc0},i} - P_{{\rm dc},i}) & \forall i \in N_n \\ V^*_{{\rm dc},j} = V_{{\rm dc0},j} + k_{f,j}(f_{{\rm on0},j} - f_{{\rm on},j}) & \forall j \in N_d \end{cases} \quad (2)$$

where, N_n is the number of onshore converters in normal operation and N_d is the number of onshore converters connected to the disturbed AC grids.

2) WFCs with CC Scheme: Fig. 3 shows the WFC control with frequency support scheme. During normal operation, the WFC creates an AC voltage with a fixed amplitude, $V_{rms,g}$, frequency, $f_{\rm off}$ and phase angle, $\theta_{\rm off}$, in order to absorb the total power generated by the wind farms.

Offshore converters use the $V_{\rm dc}$ vs. f droop to transform local DC voltage deviations, $\Delta V_{\rm dc}$, to a reference frequency signal, $f^*_{\rm off}$, using:

$$f^*_{\rm off} = f_{{\rm off},0} + k_{\rm vf}\overbrace{(V_{\rm dc0} - V_{\rm dc})}^{\Delta V_{\rm dc}}, \quad (3)$$

where $k_{\rm vf}$ is the gain of the $V_{\rm dc}$ vs. f droop control system. The measured frequency, $f_{\rm off}$, on the offshore AC network is used to activate wind turbine inertia control systems.

3) Limitations of the CC Scheme: at below rated wind speeds, wind turbines will require additional recovery power after their synthetic inertial response. The temporary underproduction of wind farm power due to wind turbine recovery power will result in a further drop of power on disturbed AC grids connected by P2P HVDC and MTDC systems equipped with the CC scheme. This will produce a further drop of frequency on the disturbed AC grid, after an initial frequency disturbance. Also, if frequency disturbances occur on different AC grids connected by an MTDC system, multiple onshore converters will use their f vs. $V_{\rm dc}$ droop controllers, as described in (2), to produce non-linear DC voltage variations. WFCs with the $V_{\rm dc}$ vs. f droop transform the DC voltage variations into an offshore frequency signal, which is used to activate synthetic inertial controllers of variable speed wind turbines. The non-linear DC voltage variations will result in maloperation of the wind turbine inertial controls, hence a telecommunications-based frequency control strategy was developed in [5], to restore the wind turbine frequency response operation on MTDC grids equipped with the CC scheme.

B. Alternative Coordinated Control Scheme

A communication-free ACC scheme is proposed to improve the effectiveness of fast frequency support from MTDC systems. The proposed ACC scheme prevents further frequency drop on disturbed AC grids during wind turbine recovery power and allows operation of wind turbine frequency control during multiple power imbalances on different AC grids. The ACC scheme is designed by fitting a supplementary frequency versus active power (f vs. P) droop control system to the GSCs and the $V_{\rm dc}$ vs. f droop (described in (3)) to the WFCs.

1) GSCs with ACC Scheme: the control operation of the GSCs is obtained by re-writing (1) as:

$$P^*_{\rm dc} = P_{\rm dc0} - k_{\rm vp}(V_{\rm dc0} - V_{\rm dc}) + k'_f(f_{\rm on0} - f_{\rm on}), \quad (4)$$

where, $k_{\rm vp} = 1/k_{\rm pv}$ and $k'_f = k_f/k_{\rm pv}$. Fig. 4 shows the control system fitted to the GSCs of the ACC scheme. When $|\Delta f_{\rm on}|$ is above $|\Delta f_{\rm db}|$, the GSCs will switch from their original droop to the f vs. P droop (where $k_{\rm vp}=0$ in (4), in order to regulate the reference value of active power, $P_{\rm dc}$, flowing through the GSCs.

The new control operation of the converters in the MTDC considering ACC is expressed as:

$$\begin{cases} P^*_{{\rm dc},i} = P_{{\rm dc0},i} - k_{{\rm vp},i}(V_{{\rm dc0},i} - V_{{\rm dc},i}) & \forall i \in N_n \\ P^*_{{\rm dc},j} = P_{{\rm dc0},j} + k'_{f,j}(f_{{\rm on0},j} - f_{{\rm on},j}) & \forall j \in N_d \end{cases} \quad (5)$$

Assuming there are no power losses in the DC grid and that no outages occur in the converter stations and given that the wind turbine synthetic inertial control is inactive, the DC voltage deviation in the MTDC grid is:

$$\Delta V^{\rm id}_{{\rm dc},w} = \frac{\sum_{i=1}^{N_d} k'_{f,i}\Delta f_{{\rm on},i}}{\sum_{i=1}^{N_n} k_{{\rm vp},i}}. \quad (6)$$

There is a linear relationship between the frequency variations, $\Delta f_{{\rm on},i}$ and the ideal DC voltage deviation, $\Delta V^{\rm id}_{{\rm dc},w}$ as in (6). This linear relationship is also true for non-ideal MTDC grids (see analysis in Appendix B and simulation results in Fig. 16a) .

2) Advantanges of the ACC Scheme: at below rated wind speeds the ACC scheme transfers wind turbine recovery power

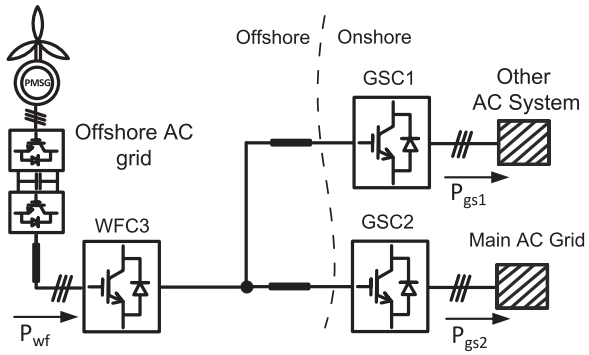

Fig. 5. 3-terminal VSC-HVDC system.

TABLE I
OPERATIONAL MODES IN A 3-TERMINAL VSC-HVDC SYSTEM

		GSC1, GSC2	WFC3
CC	Normal operation	d-axis: P vs. $V_{\rm dc}$ q-axis: Q PLL ($f_{\rm on}$)	$V_{\rm ac}$ control Oscillator ($f_{\rm off}$)
	Disturbed operation	d-axis: $f_{\rm on}$ vs. $V_{\rm dc}$ q-axis: Q PLL ($f_{\rm on}$)	$V_{\rm dc}$ vs. $f_{\rm off}$ $V_{\rm ac}$ control Oscillator ($f_{\rm off}$)
ACC	Normal operation	d-axis: $V_{\rm dc}$ vs. P q-axis: Q PLL ($f_{\rm on}$)	$V_{\rm ac}$ control Oscillator ($f_{\rm off}$)
	Disturbed operation	d-axis: $f_{\rm on}$ vs. P q-axis: Q PLL ($f_{\rm on}$)	$V_{\rm dc}$ vs. $f_{\rm off}$ $V_{\rm ac}$ control Oscillator ($f_{\rm off}$)

to undisturbed AC systems, due to the operation of the f vs. P droop in GSCs connected to disturbed AC grids. For MTDC systems with multiple frequency variations on different AC grids, the ACC scheme will enable correct operation of MTDC systems, due to the linear relationship between the frequency and the DC voltage variation in (6).

C. Example of a 3-Terminal VSC-HVDC System

A 3-terminal VSC-HVDC system is utilised to test the effectiveness of the proposed ACC scheme and the CC scheme. The HVDC system was to transfer power from an offshore wind farm to two onshore AC grids. Fig. 5 shows the 3-terminal VSC-HVDC system.

The HVDC system consists of a wind farm converter (WFC3) and two grid-side converters (GSC1 and GSC2). WFC3 interfaces the offshore wind farm to the HVDC system. GSC2 connects the HVDC system to a Main AC Grid and GSC1 connects the HVDC system to another AC system. Table I is a summary of the control modes of the GSC1, GSC2 and WFC3 during normal and disturbed operation.

Fig. 6 shows the control scheme of the offshore wind farm connected to the 3-terminal HVDC system. The network-side converter (NSC) regulates the DC link voltage and reactive power and the machine-side converter (MSC) regulates torque and reactive power [23]. The offshore frequency deviation signal, Δf_g, is used to trigger a wind turbine sythetic inertial

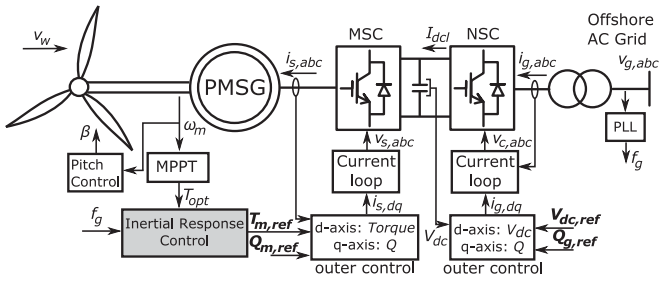

Fig. 6. Control scheme of wind turbine with fully-rated converters.

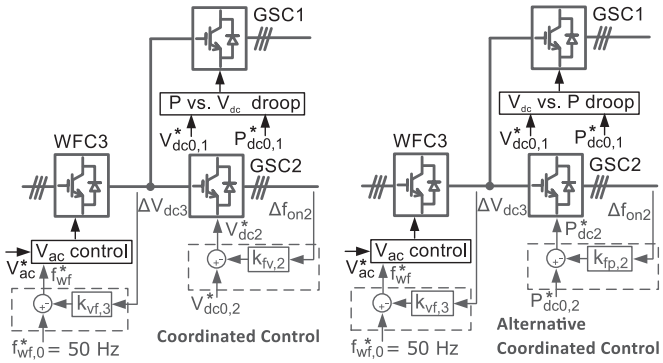

Fig. 7. Implementation of supplementary controllers during disturbed operation (a) Coordinated Control and (b) Alternative Coordinated Control.

controller that adds a torque step to the optimal value of generator torque, $T_{\rm opt}$, to produce a reference torque, $T_{m,\rm ref}$ [24].

During normal operation, the GSCs use a DC voltage droop to share power flows to the onshore AC grids and the WFC creates an AC voltage on the offshore grid. During a disturbance on the Main AC grid, the power mismatch results in a frequency deviation, $\Delta f_{\rm on2}$. The GSC2 will detect a frequency deviation above a specific margin, $f_{\rm db}$, of ± 20 mHz and switch from the original DC voltage droop to a frequency droop control. For small frequency disturbances, a hysteresis block is required to avoid repeated switching between different control modes. Large frequency disturbances (where $\Delta f_{\rm on2}$ is up to 0.5 Hz) are used to demonstrate fast frequency response from MTDC grids in this study, hence this will prevent multiple switching between control modes. Fig. 7 shows the CC and ACC scheme implementation during the disturbed operation.

1) Coordinated Control (CC): Fig. 7a shows the supplementary controls of the CC scheme. During a frequency disturbance on the Main AC grid, the GSC2 detects a frequency deviation, $\Delta f_{\rm on2}$, above ± 20 mHz and switches to an f vs. $V_{\rm dc}$ droop. The f vs. $V_{\rm dc}$ droop control is designed using:

$$V^*_{\rm dc2} = V^*_{\rm dc2,0} + k_{\rm fv,2}\Delta f_{\rm on2} = V^*_{\rm dc2,0} + \Delta V^*_{\rm dc2}, \qquad (7)$$

where $k_{\rm fv,2}$ is the gain of the f vs. $V_{\rm dc}$ droop. The output of the f vs. $V_{\rm dc}$ droop controller is a DC voltage signal, $\Delta V^*_{\rm dc2}$, which is used to compute the reference DC voltage, $V^*_{\rm dc2}$, of the GSC2 as in (7). A sample and hold block was used to measure the initial reference of DC voltage, $V^*_{\rm dc2,0}$, at the instant of

switching to the f vs. $V_{\rm dc}$ droop. At the WFC3, the DC voltage deviation, $\Delta V_{\rm dc3}$, is measured and processed by a $V_{\rm dc}$ vs. f droop controller, which is designed using:

$$f^*_{\rm wf} = f^*_{\rm wf,0} + k_{\rm vf,3}\Delta V_{\rm dc3} = f^*_{\rm wf,0} + \Delta f^*_{\rm wf}, \qquad (8)$$

where $k_{\rm vf}$ is the gain of the $V_{\rm dc}$ vs. f droop. The output of the $V_{\rm dc}$ vs. f droop controller is a frequency signal, $\Delta f^*_{\rm wf}$, which is used to regulate the set-point of frequency on the offshore AC network. At the GSC1, the DC voltage deviation, $\Delta V_{\rm dc1}$, is processed by a DC voltage droop, in order to transfer additional power from the other AC system to the disturbed AC grid.

2) Alternative Coordinated Control (ACC): Fig. 7b shows the supplementary controls of the proposed ACC scheme. During a grid disturbance on the Main AC grid, the GSC2 detects system frequency variations above ±20 mHz and switches to an f vs. P droop controller, designed using:

$$P^*_{\rm dc2} = P^*_{\rm dc2,0} + k_{\rm fp,2}\Delta f_{\rm on2} = P^*_{\rm dc2,0} + \Delta P^*_{\rm dc2}, \qquad (9)$$

where $k_{\rm fp,2}$ is the gain of the f vs. P droop. A sample and hold block was used to measure the initial set-point of active power, $P^*_{\rm dc2,0}$, at the instant of switching to the f vs. P droop. The output of the f vs. P droop is an active power signal, $\Delta P^*_{\rm dc2}$, which is used to compute the reference active power, $P^*_{\rm dc2}$, on the GSC2 as in (9). The additional active power, $\Delta P^*_{\rm dc2}$, transferred to the main AC grid through the GSC2 would result in a DC voltage deviation on the 3-Terminal HVDC system. At the WFC3, the measured DC voltage deviation, $\Delta V_{\rm dc3}$, was used to regulate the reference offshore frequency, $f^*_{\rm off}$, as in (8). At the GSC1, the DC voltage deviation, $\Delta V_{\rm dc1}$, was used by the DC voltage droop controller to transfer additional power to the main AC grid from the other AC system.

III. Simulation Model and Experimental Test Rig

The 3-terminal VSC-HVDC scheme shown in Fig. 5 was modelled using the PSCAD simulation tool. An experimental test rig was used to demonstrate the effectiveness of the CC and the proposed ACC scheme, during the wind turbine recovery period. The converters of the PSCAD simulation model and the experimental test rig are represented as two-level VSCs. The technical parameters of the simulation model and experimental test rig are found in Table V.

A. Simulation Model

The VSCs are modelled using a full switching model. The wind turbines of the offshore wind farm use Permanent Magnet Synchronous Generators (PMSG), fully controlled through back-to-back VSCs. The main objective of these converters is to generate optimum power from the wind turbines at below rated wind speed. The wind turbine inertia control system uses a step response of electromagnetic torque to extract kinetic energy from their rotating mass [24]. The Main AC Grid was modelled using a simplified GB power system model as described in [22]. The Other AC System was modelled using a three-phase AC voltage source, in order to represent a strong AC grid (e.g. Norway) with sufficient frequency support capability.

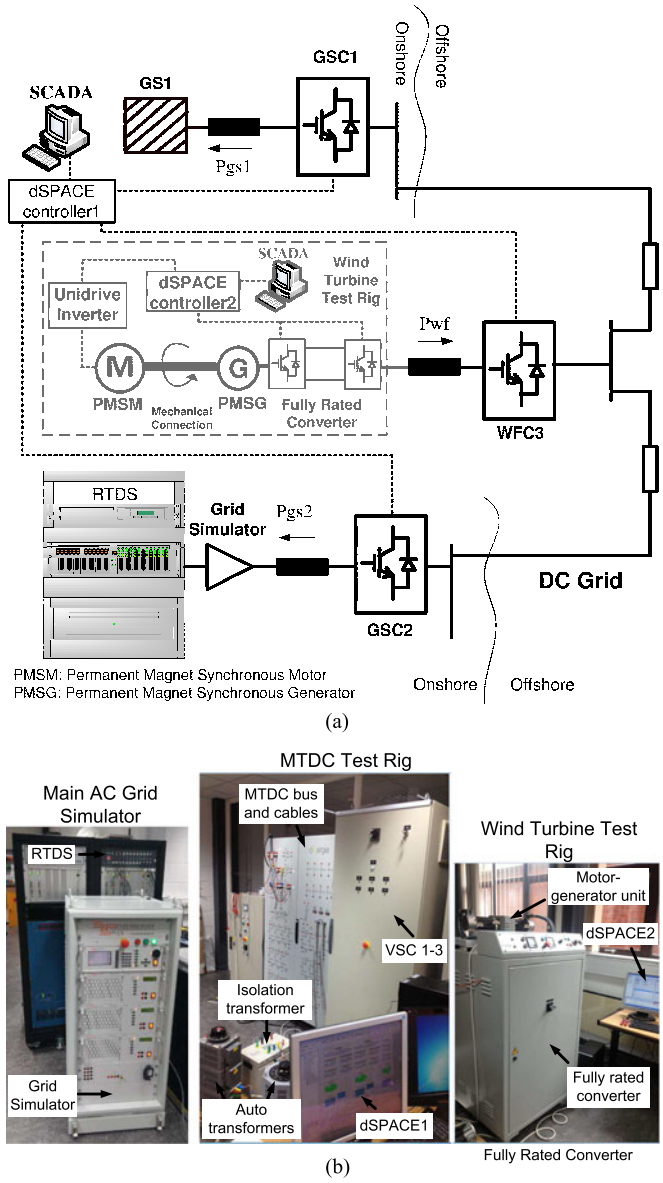

Fig. 8. Experimental test rig. (a) Schematic diagram. (b) Set-up.

B. Experimental Test Rig Components

Fig 8a shows the schematic diagram of test rig and Fig 8b shows the experimental set-up. The main components of the experimental test rig are the MTDC test rig, wind turbine test rig, real time simulator and AC grid simulator.

1) MTDC Test Rig: is formed by a VSC cabinet, autotransformer and DC network cabinet. The VSC cabinet houses three VSCs, a dSPACE controller, AC inductors and DC inductors. The VSCs operate at a rated voltage of 140 V (L-L rms) AC and 250 V DC and at a power of 2 kW. The autotransformer controls the 415 V (L-L rms) mains supply voltage of GSC1 to 140 V AC. The dSPACE controller was used to control and monitor the system states of the test rig. The DC network cabinet houses DC inductors and capacitors used to model HVDC cables.

2) Wind Turbine Rig: consists of a motor-generator set, a variable speed motor drive, two VSCs and a dSPACE controller.

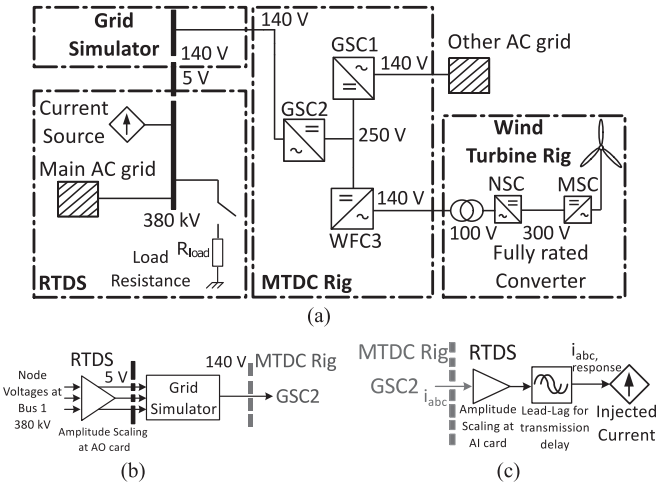

Fig. 9. Hardware-in-the-loop test. (a) Schematic diagram with operating voltages. (b) AC voltage signal transmission from the RTDS to GS to VSC test rig. (c) Current signal transmission from the VSC test rig to the RTDS.

The motor-generator set is coupled through a shaft. The variable speed motor drive uses a Unidrive inverter to control the rotational speed of the motor, in order to represent the aerodynamic and mechanical response of a real wind turbine. The two VSCs were connected to the output of the generator, using a back-to-back configuration. A dSPACE controller was used to control the VSCs and the Unidrive inverter, in order to monitor and acquire data from the test rig.

3) Real Time Simulator: a real time digital simulator (RTDS) was used to model a simplified GB power system, using the RSCAD tool of the RTDS. The GB grid was modelled as a 380 kV single-bus system with a controlled three-phase voltage source, a controlled current source and a load resistance, R_{load}, which represents a 1800 MW generation loss.

4) AC Grid Simulator: is used to interface the GB grid modelled using the RTDS to the MTDC test rig. The grid simulator (GS) is connected to the GSC2 of the MTDC test rig as shown in Fig 8a. The GS was used to achieve a conversion ratio of 380 kV/140 V, which means that an AC voltage of 140 V in the VSC test rig represents 380 kV of the high voltage system of the RTDS. Frequency disturbances on the GB grid modelled on the RTDS are measured at GSC2 by a phase locked loop (PLL), whose input is the 140 V AC voltage created by the GS. The RTDS-connected GS is used to demonstrate the impact of PLL measurement delays on the operation of MTDC frequency response control schemes.

C. Hardware-in-the-loop Tests

A hardware-in-the-loop (HIL) test was designed using the MTDC test rig, wind turbine test rig, RTDS and GS. Fig. 9a shows the schematic diagram and operating voltages of the HIL scheme. Fig. 9b shows the AC voltage signal transmitted from the RTDS to the MTDC test rig through the GS. The 380 kV AC on the GB grid modelled using the RSCAD tool of the RTDS is scaled to 5 V using the Analogue Output (AO) cards of the RTDS. The output of the AO cards is connected to the inputs of the GS. Fig. 9c shows the AC current transmitted from the VSC test rig to the RTDS through the Analogue Input (AI) cards of the RTDS. The output of the AI card was processed by a lead-lag compensator to eliminate a phase shift of 4.96 degrees between the actual VSC test rig currents, i_{abc}, the current injected to the high voltage system in the RTDS, $i_{\mathrm{abc,response}}$. The $i_{\mathrm{abc,response}}$ was the input signal to the controllable current source of the RTDS. Technical specifications of the RTDS and GS are shown in Appendix A.

TABLE II
BASE PARAMETERS OF PSCAD MODEL AND EXPERIMENTAL TEST RIG

Parameter	PSCAD Model	Test Rig
DC Voltage, $V_{\mathrm{dc},b}$	640 kV	250 V
AC Voltage, $V_{\mathrm{ac},b}$	380 kV	140 V
Active Power, P_b	1000 MW	700 W
DC impedance, $Z_{\mathrm{dc},b} = (V^2_{\mathrm{dc},b}/P_b)$	409.6 Ω	89.2 Ω
AC impedance, $Z_{\mathrm{ac},b} = (V^2_{\mathrm{ac},b}/P_b)$	144.4 Ω	28 Ω

IV. Simulation and Experimental Results

Two frequency support control schemes (CC and ACC) were modelled using the PSCAD simulation tool and implemented using the experimental test rig. Detailed models of 2-level VSC are used in the PSCAD model in order to achieve a closer representation of the experimental results. For a 1800 MW loss of generation on the main AC grid at 1 s, three cases were studied:

1) NC: no frequency support from the MTDC system
2) CC: frequency support using the CC scheme
3) ACC: frequency support using the proposed ACC scheme.

A per-unit system was utilised to scale-down the experimental test rig, in order to represent the equivalent dynamic and steady-state performance as the PSCAD model. The dynamic response of the DC test rig and PSCAD model depends on the DC cable and VSC parameters. The DC cable and VSC parameters of the experimental test rig were scaled-down to have equal per-unit values as the PSCAD model. Table II is a summary of the base values for scaling the test rig and PSCAD parameters and simulation results.

The steady-state performance of the MTDC system depends on the direct voltage droop parameters. During normal operation, the droop parameters were designed to achieve an equivalent steady-state response of DC voltage and active power (in pu) on the MTDC test rig and offline simulation models. GSC1 and GSC2 droop control parameters were chosen to transfer 0.45 pu active power to another AC system and 0.15 pu active power to the main AC grid. The droop gain k_{pv} of the P vs. V_{dc} droop is related to the droop gain k_{vp} of the V_{dc} vs. P droop using $k_{\mathrm{pv}} = 1/k_{\mathrm{vp}}$. During disturbed operation, the CC and ACC droop gains, (i.e. k_{fv} and k_{fp}) on GSC2 were chosen to transfer 0.38 pu active power to the main AC grid after frequency support. The droop gain of the f vs. P droop is expressed as $k_{fp} = k_{\mathrm{fv}}/k_{\mathrm{pv}}$. The droop parameters of the PSCAD model and experimental test rig are shown in Table IV.

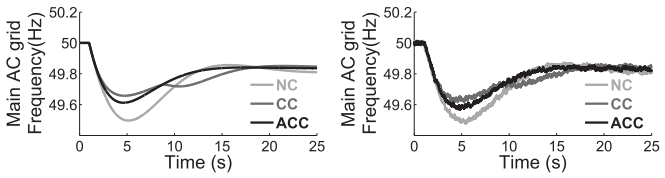

Fig. 10. Simulation (left column) and experimental (right column) results of the main ac grid frequency during the case of NC, CC and ACC.

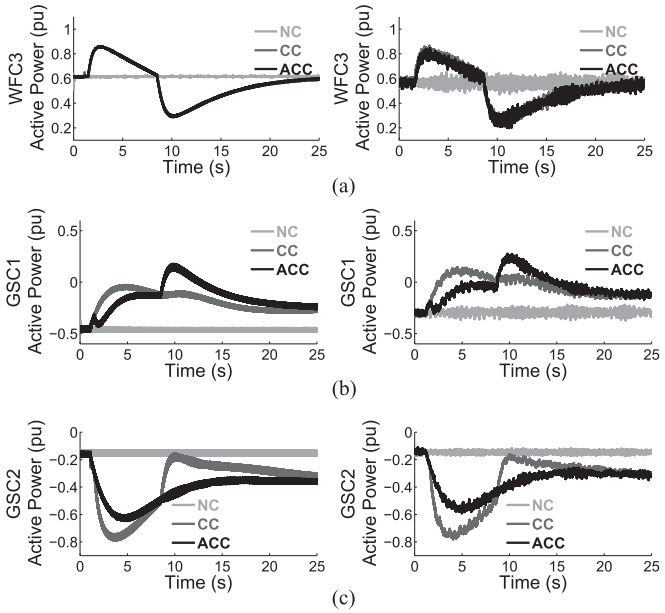

Fig. 11. Simulation (left column) and experimental (right column) results during the case of NC, CC and ACC. (a) ActiveãĂĂpower through the wind farm converter WFC3 (pu). (b) Active power through the grid side converter (GSC1) (pu). (c) Active power through the grid side converter (GSC2) (pu).

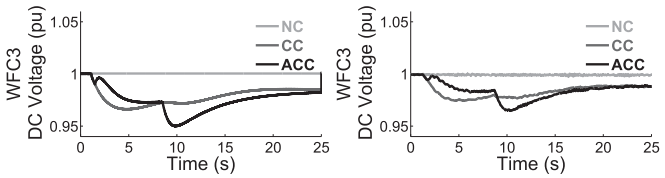

Fig. 12. Simulation (left column) and experimental (right column) results of DC voltage at the WFC3 (pu) during the case of NC, CC and ACC.

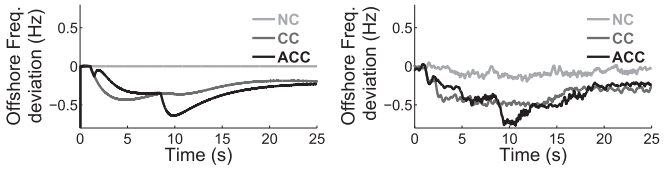

Fig. 13. Simulation (left column) and experimental (right column) of offshore AC grid frequency deviation during the case of NC, CC and ACC.

The wind turbine synthetic inertia controller was designed to transfer equal amount of extra power to the WFC3 during the case of CC and ACC. Figs. 10–13 show the simulation and experimental result of the main AC grid frequency, active power, DC voltage and offshore frequency during the case of NC, CC and ACC. There is good agreement between the simulation and experimental results. The MTDC test rig operating power (i.e. 700 W) is about 14 times less than the rated power of 10 kW. This results in no-load power losses of about 0.2 pu on the test rig, and produces an offset on the steady-state power flow on the GSC1 in Fig. 11b.

TABLE III
ROCOF OF MAIN AC GRID AND FREQUENCY DEVIATION

Case	RoCoF (Hz/s)	Δf_{on2} (Hz)
NC	0.21	0.51
CC	0.17	0.35
ACC	0.19	0.39

A. Rate of Change of Frequency and Frequency Deviation

During the period 1 s to 5 s, Fig. 10 shows that the main AC grid frequency starts to drop at time 1s, due to the 1800 MW generation loss. The rate of change of frequency (RoCoF) was measured during the period 1 s to 2 s using a sampling time of 0.5 s, as indicated in [25], and the maximum frequency deviation was measured during the period 1 s to 5 s.

Table III is a summary of the RoCoF and frequency deviation on the main AC grid. In the case of NC, the energy sources of the MTDC system did not provide frequency support. The frequency deviation has a value of 0.51 Hz, which exceeds the permissible limits on the GB grid.

For the case of CC and ACC, the MTDC system provided fast frequency response to limit the RoCoF and frequency deviation on the main AC grid compared with the case of NC. Table III shows a clear decrease of the initial RoCoF measured within 1s after the generation loss, during the case of CC and ACC. Also the frequency deviation is contained within 4 seconds after the disturbance.

In Fig. 11, a positive sign on the y-axis is used to represent the operation of the VSCs in rectifier mode and a negative sign is for the VSCs operating in inverter mode. During the case of CC, a larger amount of additional active power was transferred to the main AC grid compared with the case of ACC, as illustrated in Fig. 11c. This resulted in a lower RoCoF and a smaller frequency deviation on the main AC grid, during the case of CC compared with the case of ACC (see Table III). Also, ACC has a deeper nadir than CC (see Fig. 10), due to the f vs. P droop which limits the active power transferred through the VSCs connected to the disturbed AC grid as shown in Fig. 11c.

During the case of CC and ACC, the additional active power transferred to the main AC grid was provided from the wind turbine rotating mass (see Fig. 11a) and another AC system (see Fig. 11b). The wind turbine synthetic inertial power was delivered more rapidly than the additional active power from another AC system. Therefore, the kinetic energy taken from the wind turbines helped to limit the RoCoF and the additional power from another AC system helped to contain the frequency deviation, during the case of CC and ACC compared with the case of NC. The wind turbine auxiliary controller [24] added a 0.6 pu torque step to the initial set-point of generator torque, due to a frequency deviation signal, Δf_{wf} on the offshore network.

During the period 1 s to 2.5 s, Fig. 11a, shows that up to 0.25 pu of additional power was transferred from the wind turbine rotating mass to support the disturbed AC grid for the case of CC and ACC.

B. Wind Turbine Recovery Power

At time 8 s, the wind turbine auxiliary controller was deactivated and the reference value of generator torque was restored to its original value. During the period 8 s to 10 s, the wind turbines start to recover back to their original speed. Fig. 11a shows that the wind turbine recovery period resulted in up to 0.3 pu active power drop on the wind generation. For the case of CC, the wind turbine recovery power resulted in up to 0.3 pu active power drop on the disturbed AC grid during the period 8 s to 10 s (see Fig. 11c). This resulted in a further drop of frequency on the disturbed AC grid, as illustrated in Fig. 10. In the case of ACC, the wind turbine recovery power resulted in 0.3 pu active power increase on the other AC system during the period 8 s to 10 s as shown in Fig. 11b. This prevented a further drop of frequency on the disturbed AC grid, as shown in Fig. 10.

C. DC Voltage and Offshore Frequency Variation

Fig. 12 shows the DC voltage measured at the WFC3 during the case of NC, CC and ACC. In all the three cases, the maximum DC voltage deviation is about 0.05 pu, which is within permissible limits, assuming DC voltage limits of ± 10 percent on the MTDC system. The shape of the DC voltage curves in Fig. 12 is similar to the active power curves on the GSC1 (see Fig. 11b), due to the converter's operation with a P vs. $V_{\rm dc}$ droop.

Fig. 13 shows the AC grid frequency measured at the offshore wind farm during the case of NC, CC and ACC. The offshore frequency traces (in Fig. 13) show a proportional relation to the DC voltage traces (see Fig. 12) measured at the WFC3, due to the characteristic of the $V_{\rm dc}$ vs. f droop fitted to the WFC3. The frequency deviation, $\Delta f_{\rm wf}$, on the offshore AC network was used to activate the wind turbine inertia controller.

D. Response Times

The simulation results of GSC2 active power (see Fig. 11c) was used to analyse the response time of the frequency control schemes and energy sources, during the case of CC and ACC. For the 1800 MW generation loss at 1 s, it took 80 ms delay for the fast frequency response controllers fitted to the GSC2 to detect the generation loss. It took about 120 ms delay for the DC voltage droop controller on the GSC1 to detect the DC voltage variation, in order to transfer additional active power from another AC system to the disturbed AC grid. The activation time for the wind turbine auxiliary controller was about 500 ms after the generation loss. The maximum active power due to fast frequency response from wind turbines was delivered within 1.5 s after the generation loss.

V. Lack of Extra Power from Wind Farms

A 4-terminal VSC-HVDC system is used to demonstrate the effectiveness of the CC and ACC scheme when wind farms do not provide extra power for fast frequency response. Fig. 14 shows the 4-terminal HVDC system to transfers power from an offshore wind farm to three onshore AC grids (Grid 1, Grid 2 and Grid 3). AC Grid 1 is modelled as an infinite bus to represent a strong AC grid. AC Grid 2 and AC Grid 3 are modelled as two voltage sources with controlled frequency to represent the dynamic frequency response of GB's power system. The HVDC network consists of one WFC1 and three GSCs (GSC1, GSC2 and GSC3).

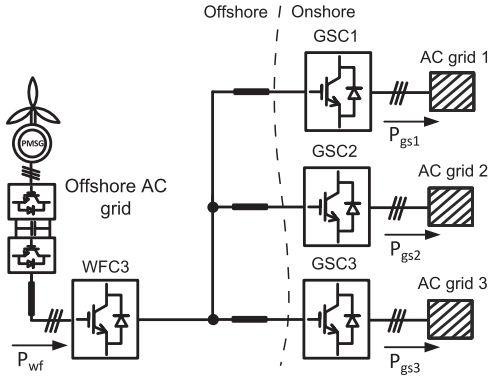

Fig. 14. 4-terminal VSC-HVDC system.

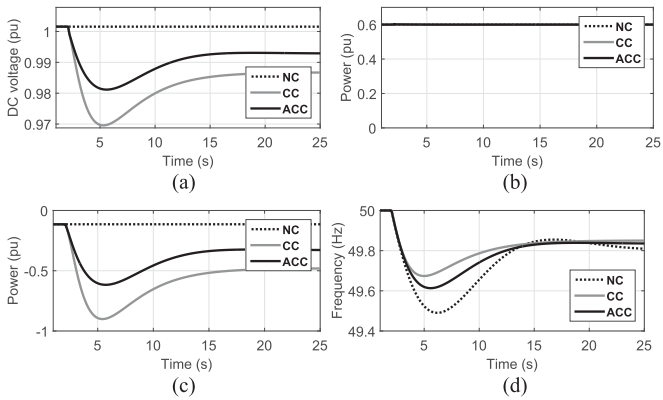

Fig. 15. Simulation results of single AC grid imbalance. (a) DC voltage on WFC3. (b) Power from Offshore Wind Farm. (c) Power on AC Grid 2. (d) Frequency on AC Grid 2.

The 4-terminal HVDC system is modelled using averaged models of 2-level VSCs in order to reduce the computational requirements of the offline simulation in MATLAB Simulink. The VSC ratings, cable parameters and frequency droop control parameters of the MTDC grid modelled using Simulink are the same as the PSCAD model used for experimental verification. The case of a single power imbalance on one AC grid and multiple power imbalances on two different AC grids were simulated in order to test the effectiveness of the CC and ACC scheme.

A. Case of single imbalance on one AC Grid

A 1800 MW generation loss on AC Grid 2 at time 1 s was utilised to demonstrate the effectiveness of the CC and ACC scheme when wind farms do not provide extra power. Fig. 15

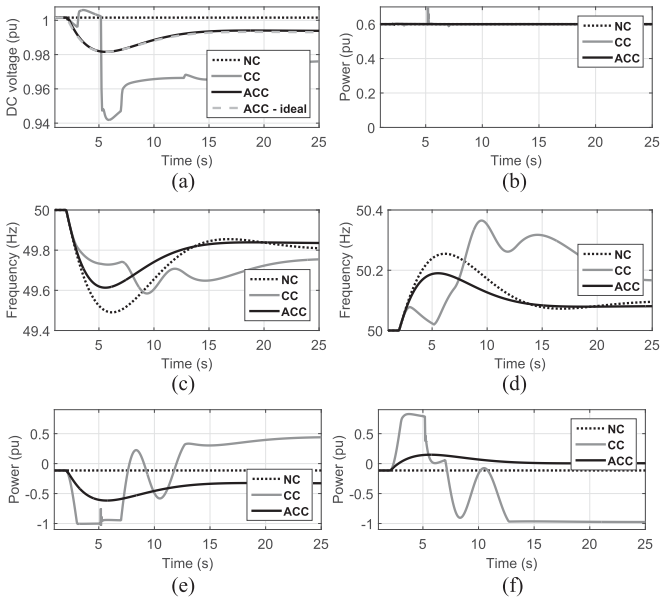

Fig. 16. Simulation results of opposing frequency trends on different AC grids. (a) DC voltage on WFC3. (b) Power from Offshore Wind Farm. (c) Frequency on AC Grid 2. (d) Frequency on AC Grid 3. (e) Power on AC Grid 2. (f) Power on AC Grid 3.

shows the curves of DC voltage, active power (at WFC3 and GSC2) and AC Grid2 frequency.

The maximum DC voltage deviation increased from 0.02 pu in the case of ACC to 0.03 pu during the case of CC as seen in Fig. 15a. For the case of NC, CC and ACC, the wind farms transfer 0.6 pu active power (see Fig. 15b) to the onshore grid. During the case of CC and ACC, the additional power for fast frequency response is taken from another AC system, due to the lack of synthetic inertial response from offshore wind farms. In Fig. 15c, more active power is transferred to AC Grid 2 in the case of CC (see grey line) compared with the case of ACC (see black line). The additional power is taken from AC Grid 1 and AC Grid 2, hence the frequency nadir in Fig. 15d is deeper during the case of ACC than the case of CC. In the case of NC, frequency support schemes were not utilized, hence the MTDC system did not provide additional active power to the disturbed AC grids, as shown in Fig. 15.

B. Case of Opposing Frequency Trends on Different AC Grids

During multiple power imbalances on different AC grids, the DC voltage in the MTDC scheme should be controlled by at least one onshore VSC during the case of CC and ACC. The CC scheme uses multiple f vs. $V_{\rm dc}$ droops on the VSCs connected to the disturbed grid. This produces non-linearity of DC voltage control, as described in (2), and results in unwanted operation of the MTDC system during frequency support. The proposed ACC scheme uses multiple f vs. P droops to achieve linear DC voltage control that allows correct operation of the MTDC system (as described in (6)). The CC and ACC schemes are tested using the case of opposing frequency trends due to a 1800 MW generation loss on AC Grid 2 and a 900 MW demand loss on AC Grid 3 at $t = 1$ s. Fig. 16 shows the WFC DC voltage, onshore frequency and active power curves (on the WFC side, AC Grid 2 and AC Grid 3) during the case of NC, CC and ACC.

For the case of ACC, Fig. 16a illustrates that the calculated DC voltage (see grey dashed line), obtained using the analytical expression in (6) for an ideal MTDC grid, has good agreement with the measured DC voltage (see black solid line) on the non-ideal MTDC grid modelled in Simulink. This demonstrates the linear relationship between the frequency variations in Fig. 16c and Fig. 16d and the DC voltage, due the operation of two GSCs with the f vs. P droop. Hence, the ACC scheme will facilitate the operation of wind turbine inertia controllers.

For the CC scheme, a non-linear relationship exists between the DC grid voltage and the onshore AC grid frequencies, as described in (2), due to the operation of the f vs. $V_{\rm dc}$ droop controller on the GSC2 and GSC3. Fig. 16a illustrates that the DC voltage (see grey solid line) is not controlled properly due to multiple DC voltage control operation on the MTDC system during power imbalances on AC Grid 2 and AC Grid 3. The DC voltage response will result in incorrect operation of wind turbine inertia controllers Figs. 16c -16f shows that the CC scheme results in larger power oscillations and frequency deviations on AC Grid 2 and AC Grid 3 compared with the ACC scheme.

VI. Conclusions

A communication-free alternative coordinated control (ACC) scheme is developed to prevent further frequency drop on disturbed AC grids during wind turbine recovery period. Also, the proposed ACC scheme allows correct operation of fast frequency response from MTDC-connected wind farms during multiple power imbalances on different AC grids, due to the linear relationship between the MTDC voltage and the onshore AC grid frequencies. The ACC scheme, which gives priority to the frequency versus active power droop on VSCs connected to disturbed AC grids, is compared with a coordinated control (CC) scheme presented in the literature, which uses a frequency versus DC voltage droop. During a single power imbalance in one AC grid, fast frequency response from MTDC-connected wind farms (equipped with the ACC and CC scheme) limits the RoCoF on disturbed AC grids and additional active power transferred from another AC system contains the system frequency deviation. This will prevent unintended tripping of protection relays on power systems and enhance the frequency control requirements of AC grids.

Appendix A
RTDS and Grid Simulator

RTDS: 1 Rack. Cards: 1 GTWIF. 4 GPC (2 IBM PPC750GX 1 GHz), 1 GTIRC, 1 GTDI, 1 GTDO, 1 GTAI, 1 GTAO, 1 GTNET.

Single-bus system: Base Voltage: 380 kV; Base Power: 1000 MVA; Base frequency, $f_b = 50$ Hz; Load resistance: $R_f = 81$ Ω; Load = 1800 MW; Time step = 50 μs;

Signal Transmission: RTDS $\rightarrow$ MTDC, voltage factor 0.35; MTDC $\rightarrow$ RTDS, current factor 1.2; Lead-lag compensator: gain $K_{L-L} = 0.917$, time constants: $\tau_{\rm Lead} = 0.0034$, $\tau_{\rm Lag} = 0.0029$.

TABLE IV
PARAMETERS OF SUPPLEMENTARY CONTROLLERS

		k_{fv}	k_{pv}	k_{vf}	k_{fp}
Simulation	CC	65	0.05	0.02	-
	ACC	-	0.05	0.02	1300
Experiment	CC	20	0.02	0.07	-
	ACC	-	0.02	0.07	1000

TABLE V
MTDC AND WIND TURBINE PARAMETERS

		Simulation	Experiment
DC Cables	L_{gs1-wf}	43.12 mH	9.4 mH
	L_{wf-gs2}	11.01 mH	2.4 mH
	R_{gs1-wf}	1.0752 Ω	0.2344 Ω
	R_{wf-gs2}	0.2048 Ω	0.045 Ω
Converters	Operated Power	1000 MW	700 W
	AC Voltage	380 kV	140 V
	DC Voltage	±320 kV	±125 V
	DC Capacitor	223.26 μF	1020 μF
	AC inductor	11.35 mH	2.2 mH
Wind Turbine	Poles pairs	125	2
	Wind speed	10.2 m/s	10.2 m/s
	Rotor speed	1.4 rpm	2050 rpm
	Coherent machines	200	-
	Inertia	$30{\cdot}10^6$ kg · m^2	2.9 kg · cm^2
	Operated Power	5 MVA	700 VA
	AC Voltage	690 V	100 V
	DC Voltage	±600 V	±150 V

Grid Simulator: 4-quad. amp; Rating: cont. 1 kVA, short-time 2 kVA; Nom. Volt.: ac 270 Vrms, dc ±382 V; Input: Max. voltage ±5Vp; Impedance ≈ 8 kΩ; Slew rate > 52 V/μs; Power supply: 230 V; Protection: 16 A.

APPENDIX B
DC VOLTAGE ON NON-IDEAL MTDC GRIDS WITH ACC

The DC voltage deviation can be calculated from the sum of exchanged power between converters in small-signal form:

$$\sum_{i=1}^{N} \Delta P_i = \Delta P_{\mathrm{losses}} \tag{10}$$

The sum of exchanged power can be expressed as:

$$\sum_{i=1}^{N} \Delta P_i = \overbrace{\sum_{i=1}^{N_n} k_{\mathrm{vp},i} \Delta V_{\mathrm{dc},i}}^{V_{\mathrm{dc}} \text{ vs. } P \text{ droop}} - \overbrace{\sum_{i=1}^{N_d} k_{f,i}^{'} \Delta f_{\mathrm{on},i}}^{f \text{ vs. } P \text{ droop}} \tag{11}$$

and the total power losses are:

$$\Delta P_{\mathrm{losses}} = \sum_{i=1}^{N} 2 I_{\mathrm{iw},o} R_{\mathrm{iw}} \Delta I_{\mathrm{iw}} \tag{12}$$

where, $I_{\mathrm{iw},o}$ and ΔI_{iw} are the initial current and current variation from onshore converter i to offshore converter w and R_{iw} is the equivalent resistance from onshore converter i to offshore converter w.

Combining (10)–(12) and considering the voltage drop between onshore converters and WFC, $\Delta V_{\mathrm{dc},w} = \Delta V_{\mathrm{dc},i} + R_{\mathrm{iw}} \Delta I_{\mathrm{iw}}$, the DC voltage deviation at the WFC is:

$$\Delta V_{\mathrm{dc},w} = \overbrace{\frac{\sum_{i=1}^{N_d} k_{f,i}^{'} \Delta f_{\mathrm{on},i}}{\sum_{i=1}^{N_n} k_{\mathrm{vp},i}}}^{\Delta V_{\mathrm{dc},w}^{\mathrm{id}}} + \overbrace{\frac{\sum_{i=1}^{N_n} k_{\mathrm{vp},i} \Delta I_{\mathrm{iw}} R_{\mathrm{iw}}}{\sum_{i=1}^{N_n} k_{\mathrm{vp},i}}}^{\Delta V_{\mathrm{dc},w}^{\mathrm{vdrop}}} + \overbrace{\frac{\sum_{i=1}^{N} 2 I_{\mathrm{iw},o} \Delta I_{\mathrm{iw}} R_{\mathrm{iw}}}{\sum_{i=1}^{N_n} k_{\mathrm{vp},i}}}^{\Delta V_{\mathrm{dc},w}^{\mathrm{losses}}} \tag{13}$$

where $\Delta V_{\mathrm{dc},w}^{\mathrm{losses}}$ is the additional DC voltage deviation due to the voltage drop between onshore converters and WFC and $\Delta V_{\mathrm{dc},w}^{\mathrm{vdrop}}$ is the additional DC voltage deviation due to power losses. If a lossless MTDC grid is considered, $\Delta P_{\mathrm{losses}} = 0$, $\Delta V_{\mathrm{dc},w} = \Delta V_{\mathrm{dc},i}$ and the DC voltage deviation corresponds to $\Delta V_{\mathrm{dc},w}^{\mathrm{id}}$. As an example, the DC voltage deviation in the 3-terminal case study presented in section II-C is calculated when a frequency disturbance occurs in Main AC grid. In this case, $\Delta I_{\mathrm{iw}} = \Delta P_i / V_{\mathrm{dc},i}$, due to the radial topology of the MTDC grid. Then, (13) is expressed as:

$$\Delta V_{\mathrm{dc},3} = \frac{k_{f,2}^{'} \Delta f_{\mathrm{on},2}}{k_{\mathrm{vp},1}} + \frac{k_{\mathrm{vp},1} \Delta V_{\mathrm{dc},1} R_{13}}{V_{\mathrm{dc},1}} + \frac{2 I_{13,o} R_{13} k_{\mathrm{vp},1} \Delta V_{\mathrm{dc},1} / V_{\mathrm{dc},1} - 2 I_{23,o} R_{23} k_{f,2}^{'} \Delta f_{\mathrm{on},2} / V_{\mathrm{dc},2}}{k_{\mathrm{vp},1}} \tag{14}$$

The non-ideal additional terms can be negligible for nominal operational conditions. Considering the simulation parameters in Table IV, the simulation base values in Table II and maximum DC voltage and frequency deviations equal to $\Delta V_{\mathrm{dc,max}} = 0.1$ pu and $\Delta f_{\mathrm{on,max}} = 0.8$ Hz, the maximum DC voltage deviation at WFC3 is estimated as:

$$\begin{aligned} \Delta V_{\mathrm{dc},3}^{\mathrm{nid}} &= \Delta V_{\mathrm{dc},3}^{\mathrm{id}} + \Delta V_{\mathrm{dc},3}^{\mathrm{vdrop}} + \Delta V_{\mathrm{dc},3}^{\mathrm{losses}} \\ &= 0.081 + 0.0034 + 0.0004 = 0.0848 \text{ pu} \end{aligned} \tag{15}$$

It is observed that the additional terms can be neglected, because they only represent 0.38% of the nominal voltage. Also, the main contribution in the additional non-ideal terms is from the voltage drop between converters. This is due to the inherent error in the proportional characteristic of the onshore droop controllers. The voltage drop effect on the non-ideal DC voltage deviation can be reduced if higher droop gains $k_{\mathrm{vp},i}$ are used.

ACKNOWLEDGEMENT

Information about the data upon which the reported results are based, including how to access them, can be found in the Cardiff University data catalogue at http://doi.org/10.17035/d.2016.0011647652.

REFERENCES

[1] National Grid, System operability framework 2015, Warwick, U.K., 2015. [Online]. Available: http://www2.nationalgrid.com/UK/Industry-information/Future-of-Energy/System-Operability-Framework/

[2] J. Ekanayake and N. Jenkins, "Comparison of the response of doubly fed and fixed-speed induction generator wind turbines to changes in network frequency," *IEEE Trans. Energy Convers.*, vol. 19, no. 4, pp. 800–802, Dec. 2004.
[3] G. C. Tarnowski, P. C. Kjar, P. E. Sorensen, and J. Ostergaard, "Variable speed wind turbines capability for temporary over-production," in *Proc. IEEE Power Energy Soc. Gen. Meeting*, Jul. 2009, pp. 1–7. [Online]. Available: http://ieeexplore.ieee.org/lpdocs/epic03/wrapper.htm?arnumber=5275387
[4] National Grid, Electricity ten year statement (ETYS) 2015, 2015. [Online]. Available: http://www2.nationalgrid.com/UK/Industry-information/Future-of-Energy/Electricity-Ten-Year-Statement/
[5] I. M. Sanz, B. Chaudhuri, and G. Strbac, "Inertial response from offshore wind farms connected through DC grids," *IEEE Trans. Power Syst.*, vol. 30, no. 3, pp. 1518–1527, May 2015.
[6] A. Junyent-Ferre, Y. Pipelzadeh, and T. C. Green, "Blending HVDC-link energy storage and offshore wind turbine inertia for fast frequency response," *IEEE Trans. Sustain. Energy*, vol. 6, no. 3, pp. 1059–1066, Jul. 2015.
[7] L. Chang-Chien, W. Lin, and Y. Yin, "Enhancing frequency response control by DFIGs in the high wind penetrated power systems," *IEEE Trans. Power Syst.*, vol. 26, no. 2, pp. 710–718, May 2011.
[8] D. Gautam, L. Goel, R. Ayyanar, V. Vittal, and T. Harbour, "Control strategy to mitigate the impact of reduced inertia due to doubly fed induction generators on large power systems," *IEEE Trans. Power Syst.*, vol. 26, no. 1, pp. 214–224, Feb. 2011.
[9] J. Morren, S. de Haan, W. Kling, and J. Ferreira, "Wind turbines emulating inertia and supporting primary frequency control," *IEEE Trans. Power Syst.*, vol. 21, no. 1, pp. 433–434, Feb. 2006.
[10] National Grid, Grid code frequency response technical sub-Group report, 2013. [Online]. Available: http://www2.nationalgrid.com/UK/Industry-information/Electricity-codes/Grid-code/Modifications/GC0022/
[11] National Grid, SMART frequency control project—The balance of power, 2015. [Online]. Available: http://www.nationalgridconnecting.com/The_balance_of_power/index.html
[12] J. Guerrero, G. Adam, and C. Booth, "A generic inertia emulation controller for multi-terminal VSC–HVDC systems," in *Proc. 2nd IET Renew. Power Gener. Conf.*, 2013, p. 2.14.
[13] Y. Phulpin, "Communication-free inertia and frequency control for wind generators connected by an HVDC-link," *IEEE Trans. Power Syst.*, vol. 27, no. 2, pp. 1136–1137, May 2012.
[14] J. Zhu, C. D. Booth, G. P. Adam, A. J. Roscoe, and C. G. Bright, "Inertia emulation control strategy for VSC–HVDC transmission systems," *IEEE Trans. Power Syst.*, vol. 28, no. 2, pp. 1277–1287, May 2013.
[15] Y. Li, Z. Zhang, Y. Yang, Y. Li, H. Chen, and Z. Xu, "Coordinated control of wind farm and VSC–HVDC system using capacitor energy and kinetic energy to improve inertia level of power systems," *Int. J. Elect. Power Energy Syst.*, vol. 59, pp. 79–92, Jul. 2014.
[16] B. Silva, C. L. Moreira, L. Seca, Y. Phulpin, and J. A. Pecas Lopes, "Provision of inertial and primary frequency control services using offshore multiterminal HVDC networks," *IEEE Trans. Sustain. Energy*, vol. 3, no. 4, pp. 800–808, Oct. 2012.
[17] T. M. Haileselassie and K. Uhlen, "Power system security in a meshed north sea HVDC grid," *Proc. IEEE*, vol. 101, no. 4, pp. 978–990, Apr. 2013.
[18] N. R. Chaudhuri, R. Majumder, and B. Chaudhuri, "System frequency support through multi-terminal DC (MTDC) grids," *IEEE Trans. Power Syst.*, vol. 28, no. 1, pp. 347–356, Feb. 2013.
[19] P. Rault, X. Guillaud, F. Colas, and S. Nguefeu, "Investigation on interactions between AC and DC grids," in *Proc. IEEE Grenoble Conf.*, Jun. 2013, pp. 1–6.
[20] S. Akkari, M. Petit, J. Dai, and X. Guillaud, "Interaction between the voltage-droop and the frequency-droop control for multi-terminal HVDC systems," *IET Gen., Transm. Distrib.*, vol. 10, no. 6, pp. 1345–1352, Apr. 2016.
[21] L. Xu, J. Rafferty, Y. Wang, and G. Xu, "MTDC systems for frequency support base on dc voltage manipulation," in *Proc. Int. Conf. Renew. Power Gen.*, 2015, p. 6.
[22] Y. Mu, J. Wu, J. Ekanayake, N. Jenkins, and H. Jia, "Primary frequency response from electric vehicles in the Great Britain power system," *IEEE Trans. Smart Grid*, vol. 4, no. 2, pp. 1142–1150, Jun. 2013.
[23] M. Cheah-Mane, J. Liang, and N. Jenkins, "Permanent magnet synchronous generator for wind turbines: Modelling, control and inertial frequency response," in *Proc. 49th Int. Univ. Power Eng. Conf.*, Sep. 2014, pp. 1–6.
[24] M. Kayikci and J. Milanovic, "Dynamic contribution of DFIG-based wind plants to system frequency disturbances," *IEEE Trans. Power Syst.*, vol. 24, no. 2, pp. 859–867, May 2009.
[25] European Network of Transmission System Operators—Electricity, "Draft network code on high voltage direct current connections and DC-connected power park modules," ENTSO-E, Brussels, Belgium, 2014.

Oluwole Daniel Adeuyi (S'11–M'16) received the B.Sc. degree in electrical/electronics engineering from the Federal University of Agriculture, Abeokuta, Nigeria, in 2010, the M.Sc. degree (Hons.) in 2012, and the Ph.D. degree in electrical energy systems from Cardiff University, Cardiff, U.K., in 2016.

He is a Research Fellow in the School of Engineering, Cardiff University, with a focus on enhanced control and operation of renewable energy systems, offshore dc networks, and smart power grids.

Marc Cheah-Mane (S'14) received the degree in industrial engineering from the School of Industrial Engineering of Barcelona, Technical University of Catalonia, Barcelona, Spain, in 2013 and is currently pursuing the Ph.D. degree at Cardiff University, Cardiff, U.K.

From 2010 to 2013, he was a Researcher in the Centre d'Innovacio Tecnologica en Convertidors Estatics i Accionaments. His research interests include renewable energies, power converters, high-voltage dc systems, electrical machines, and microgrids.

Jun Liang (M'02–SM'12) received the B.Sc. degree in electrical power engineering from Huazhong University of Science and Technology, Wuhan, China, in 1992 and the M.Sc. and Ph.D. degrees from the China Electric Power Research Institute, Beijing, China, in 1995 and 1998, respectively.

From 1998 to 2001, he was a Senior Engineer with the China Electric Power Research Institute. From 2001 to 2005, he was a Research Associate in the Imperial College London, London, U.K. From 2005 to 2007, he was a Senior Lecturer at the University of Glamorgan, Pontypridd, U.K.

He is currently a Reader in the School of Engineering, Cardiff University, Cardiff, U.K. His research interests include FACTS devices/HVdc, power system stability and control, power electronics, and renewable power generation.

Nick Jenkins (M'81–SM'97–F'05) received the B.Sc. degree from Southampton University, Southampton, U.K., in 1974, the M.Sc. degree from Reading University, Reading, U.K., in 1975, and the Ph.D. degree from Imperial College London, London, U.K., in 1986.

He is currently a Professor and Director in the Institute of Energy, Cardiff University, Cardiff, U.K. Before moving to academia, his career included 14 years of industrial experience, of which five years were in developing countries. While at the university, he has developed teaching and research activities in both electrical power engineering and renewable energy.